Materials & Design 222 (2022) 111018

Contents lists available at ScienceDirect

Materials & Design

journal homepage: www.elsevier.com/locate/matdes

Improved light-weighting potential of SS316L triply periodic minimal surface shell lattices by micro laser powder bed fusion

Jin Fu [a], Junhao Ding [b], Shuo Qu [b], Lei Zhang [c], Michael Yu Wang [c], M.W. Fu [a,*], Xu Song [b,*]

[a] Department of Mechanical Engineering, Research Institute for Advanced Technology, The Hong Kong Polytechnic University, Hung Hom, Kowloon, Hong Kong, China
[b] Department of Mechanical and Automation Engineering, Chinese University of Hong Kong, Shatin, Hong Kong, China
[c] Department of Mechanical and Aerospace Engineering, Hong Kong University of Science and Technology, Clear Water Bay, Kowloon, Hong Kong, China

HIGHLIGHTS

- Micro laser powder bed fusion (μLPBF) was used to fabricate lightweight triply periodic minimal surfaces (TPMS) structures.
- The TPMS structures fabricated by μLPBF demonstrate superior light-weighting potential for mechanical applications compared with conventional LPBF.
- The deformation mode of TPMS structures transforms from localized collapse to homogeneous bulk deformation with increasing relative density.
- Primitive TPMS shows the highest anisotropy in compressive responses, while Gyroid TPMS suggests a near-isotropic behavior.
- Diamond TPMS with [100] orientation exhibits a superior scaling behavior and the best combination of stiffness, strength and toughness.

GRAPHICAL ABSTRACT

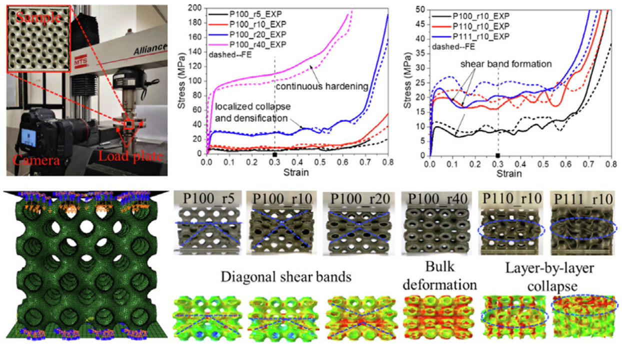

ARTICLE INFO

Article history:
Received 3 April 2022
Revised 26 June 2022
Accepted 1 August 2022
Available online 3 August 2022

Keywords:
Triply periodic minimal surface
Micro laser powder bed fusion
Deformation mechanism
Energy absorption
Light-weighting potential

ABSTRACT

Micro laser powder bed fusion (μLPBF), for the first time, enables fabrication of low-density triply periodic minimal surface (TPMS) shell lattices with smaller feature size. However, the understandings on the mechanical responses of lightweight TPMS structures by μLPBF are yet to be updated. Herein, stainless steel 316L TPMS shell lattices (i.e., Primitive (P), Diamond (D) and Gyroid (G)) with different shell thicknesses and cell orientations were fabricated by μLPBF. Low-density TPMS structures with shell thickness as small as ~100 μm and relative density ~5 % were realized. Quasi-static compression tests and finite element modelling were conducted to study their compressive responses. Their light-weighting potential related to the scaling behavior of mechanical properties as a function of relative density was analyzed. Results show with increasing relative density, the deformation mechanism transforms from localized collapse to homogeneous bulk deformation. P-type TPMS exhibits the highest anisotropy of stiffness, strength and energy absorption capability, while G-type TPMS is near-isotropic. [100] oriented D-type TPMS shows the highest strength and best light-weighting potential. Compared with conventional LPBF, the μLPBF TPMS structures demonstrate higher mechanical properties and superior

---

* Corresponding authors.
E-mail addresses: mmmwfu@polyu.edu.hk (M.W. Fu), xsong@cuhk.edu.hk (X. Song).

https://doi.org/10.1016/j.matdes.2022.111018
0264-1275/

light-weighting potential. Overall, this work highlights the superiority of the μLPBF technology in fabricating lightweight TPMS structures for mechanical applications.

1. Introduction

Recently, the advancement of additive manufacturing technology gives rise to a new type of "periodic + open cell" shell-based lattice structure [1] - Triply Periodic Minimal Surfaces (TPMS) based lattices. They are surfaces that locally minimize the surface area for a given boundary such that the mean curvature at each point on the surface is zero [2]. These surfaces have distinctive geometrical characteristics, such as the smooth surface, controllable pore size and interconnected subdomains [3]. These shell-based (or so-called shellular/sheet-network) TPMS structure models are created by thickening the surfaces [1]. They are different from the skeletal (or so-called solid-network) TPMS structures, which are generated by solidifying the volume on one side of the surfaces [4]. Various studies [5–8] have reported that sheet TPMS structures exhibit superior mechanical properties than both skeletal TPMS structures and strut-based lattice structures. Moreover, although plate-based lattice structures can reach the theoretical limits of stiffness and yield strength [9], their energy absorption capability is proven to be inferior to the shell-based TPMS structures due to smaller plateau strength and individually collapse of sublayers [10]. Therefore, metallic TPMS shell lattices are promising candidates for load-bearing and energy absorption applications [3].

Although TPMS geometries were created many years ago, their fabrication was not achieved due to the limitations of traditional manufacturing technologies. Recent advancements in Additive Manufacturing (AM) facilitate this task and allow complex TPMS geometries to be made. Based on the existing review [3,11], Laser Powder Bed Fusion (LPBF), or commonly known as Selective Laser Melting, is the most reported AM technique for manufacturing metallic TPMS lattices for industrial applications. Compared with the blown powder and material deposition AM methods, LPBF is able to create more complex structures due to the powder bed support. In addition, the continuous and open-cell nature of the TPMS structures makes the powder removal easy after printing. However, current LPBF systems are only able to make the structure with the minimum feature size of ~200 μm [12], which may not be able to provide satisfactory geometrical precision, and also limits the light-weighting potential of TPMS shell lattices.

To improve the printing precision, a micro LPBF (μLPBF) system has been tailor-made based on Han's Laser machine frame M100 equipped with laser beam diameter of <= 25 μm, which can achieve and minimum feature size of ~50 μm. Various metals and alloys have been successfully printed using the μLPBF equipment [13–15]. Benefiting from the development of μLPBF technology, lightweight TPMS shell lattices with smaller shell thickness and higher surface quality can be easily fabricated [16,17]. On the other hand, different materials have been used for evaluating the mechanical properties of the sheet-based TPMS structures, such as aluminum alloy [18], titanium alloy [19] and steel [6,10]. Stainless steel (SS) is often chosen for the mechanical evaluation of TPMS due to its capability to accommodate large plastic deformation to allow the TPMS structures crushing to full densification [6,10,20]. Our previous study indicated that the material SS316L fabricated by μLPBF has finer microstructure, desired mechanical properties and smaller part distortion, as compared with the counterpart by conventional LPBF [21]. Therefore, the μLPBF of SS316L offers great advantage to explore the light-weighting potential of TPMS shell lattices and the possible variation of mechanical response in the low relative density.

A comprehensive summary of the values for Young's modulus, yield strength and plateau strength of TPMS structures was provided by Al-Ketan and Abu Al-Rub [3] for different constituent materials, relative densities and topologies. The combination of numerical and experimental study is quite efficient to fully understand the mechanical behavior of TPMS structures. Specifically, the elastic and yield properties of TPMS shell lattices can be numerically investigated using single tessellating cell with periodic or mixed boundary conditions to avoid expensive computational cost [22–25]. In contrast, the plastic deformation and mechanical energy absorption are usually non-periodic and non-local, which has to be investigated using a full-scale model containing enough tessellating cells to capture post-yield behavior [26]. To date, there have been many publications on the large plastic deformation and mechanical energy absorption of sheet-based TPMS structures, and effect of TPMS cell type [6], Z-direction functional gradient [27], relative density [6] and TPMS design variations [28] are studied. Furthermore, energy absorption diagrams for different cell types were developed for the selection of TPMS structures and relative densities [6]. Fabricated by the conventional LPBF, however, the relative density $\bar{\rho}$ of TPMS samples is limited by the minimum printable wall thicknesses, with only $\bar{\rho}$ over 12 % and shell thickness over 200 μm studied. For the relative density range of 10–30 %, it was reported that the deformation behavior of TPMS structures is independent on the relatively density [6]. Bonatti and Mohr highlighted the anisotropic elastic and plastic properties of TPMS-like shell lattices [29]. TPMS-like structures with a wide range of $\bar{\rho}$ from 1 % to 80 % were studied mainly based on numerical simulation, in which samples with relative densities ranging 10–30 % were experimentally validated. However, the low-density TPMS shell lattices (such as 1 % $\bar{\rho}$) are difficult to fabricate by current metal AM technology due to the printing resolutions. Here, there is little experimental research on the compressive behavior and the anisotropy of TPMS shell lattices with relative densities lower than 10 % in the literature. The emerging advanced μLPBF technologies enable the comprehensive experimental and numerical investigations on the mechanical properties and their orientation dependency of these low-density lattice structures, facilitating their lightweight applications in the unexplored low-density regions.

In this work, TPMS shell lattices (i.e., Primitive (P), Diamond (D) and Gyroid (G)) with different shell thicknesses (with predefined relative density ranging from 5 % ~ 40 %) and cell orientations ([1 0 0], [1 1 0] and [1 1 1] along loading direction) were fabricated by μLPBF of SS316L powders. The manufacturability of the TPMS shell lattices by μLPBF was also studied in terms of the surface quality, measured relative density and shell thickness. Quasi-static compression tests and finite element (FE) modelling were conducted to study the deformation modes, mechanical properties and energy absorption capability of TPMS structures considering the effects of TPMS types, relative densities, and loading directions. The improved light-weighting potential of the μLPBF TPMS structures related to the scaling of mechanical properties as a function of relative density was demonstrated and analyzed.

2. Numerical and experimental methods

2.1. Implicit design and additive manufacturing

The geometry of TPMS lattices can be described by implicit nodal approximation [30]. Level-set functions $\varnothing(x,y,z)=c$ are widely used equations for TPMS generation. The typical examples, including Primitive (P), Diamond (D) and Gyroid (G) lattices, can be expressed as follows:

$$\varnothing_P = cos(wx) + cos(wy) + cos(wz) = c \tag{1a}$$

$$\varnothing_G = cos(wx)sin(wy) + cos(wy)sin(wz) + cos(wz)sin(wx) = c \tag{1b}$$

$$\varnothing_D = \sin(wx)\sin(wy)\sin(wz) + \sin(wx)\cos(wy)\cos(wz) + cos(wx)sin(wy)cos(wz) + cos(wx)cos(wy)sin(wz) = c \tag{1c}$$

where x, y, z are spatial coordinates, $w = 2\pi/L$ and L is the side length of a unit cell. The level c controls the pore size of the TPMS unit cell. The G-, D-, P-type TPMS models are created by extracting surfaces using the above equations with c defined as zero. By uniformly thickening the middle surface, TPMS shell lattices with uniform thickness can be constructed. In contrast, it should be noted the method by filling the domain between the two surfaces $\varnothing(x,y,z)=\pm c$ creates a sheet TPMS structure with non-uniform shell thickness.

To study the effect of cell orientation on the compressive properties, we consider the three main cubic directions, namely, [1 0 0], [1 1 0] and [1 1 1]. The equations (1 a, b and c) are used for generating G-, D-, P-type TPMS models with [1 0 0] direction only. To generate TPMS models with [1 1 0] and [1 1 1] directions, the Rodrigues formulae are employed to rotate the global coordinates [31], which can be expressed as:

$$\boldsymbol{v}_{rot} = \boldsymbol{R}\boldsymbol{v} \tag{2a}$$

$$\boldsymbol{R} = \boldsymbol{E}cos\theta + (1-cos\theta)\boldsymbol{k}\boldsymbol{k}^T + sin\theta\begin{bmatrix} 0 & -k_z & k_y \\ k_z & 0 & -k_x \\ -k_y & k_x & 0 \end{bmatrix} \tag{2b}$$

where $\boldsymbol{R}$ is the Rodrigues matrix for rotation, $\boldsymbol{E}$ is the 3rd order identity matrix, $\boldsymbol{v}_{rot}$ is the rotated vector ($[110]^T$or$[111]^T$), $\boldsymbol{v}$ is the vector to be rotated ($[100]^T$), $\boldsymbol{k} = \begin{bmatrix} k_x & k_y & k_z \end{bmatrix}^T$ is a unit vector describing the rotation axis, and θ is the rotation angle. $\boldsymbol{k}$ and θ can be calculated as:

$$\theta = -\arccos\frac{\boldsymbol{v}_{rot}\cdot\boldsymbol{v}}{|\boldsymbol{v}_{rot}||\boldsymbol{v}|} \tag{2c}$$

$$\boldsymbol{k} = \frac{\boldsymbol{v}_{rot}\times\boldsymbol{v}}{|\boldsymbol{v}_{rot}\times\boldsymbol{v}|} \tag{2d}$$

In this work, the side length 4 mm of [1 0 0] unit cell is chosen. Cubic TPMS specimens with dimension of 16 × 16 × 16 mm^3 are constructed, which contains 4 × 4 × 4 tessellating cells for [1 0 0] specimens and can provide a mechanical behavior close to an infinite array [28,32–34]. Because of the larger size of [1 1 0] and [1 1 1] unit cell [29], the specimen volume of 16 × 16 × 16 mm^3 doesn't contain 4 × 4 × 4 unit cells for [1 1 0] and [1 1 1]. Our preliminary numerical studies have proved that the volume of 16 × 16 × 16 mm^3 was sufficient to provide representative results for [1 0 0], [1 1 0] and [1 1 1] directions. Matlab script is used to generate the 3D stereo-lithography (STL) models of TPMS structures

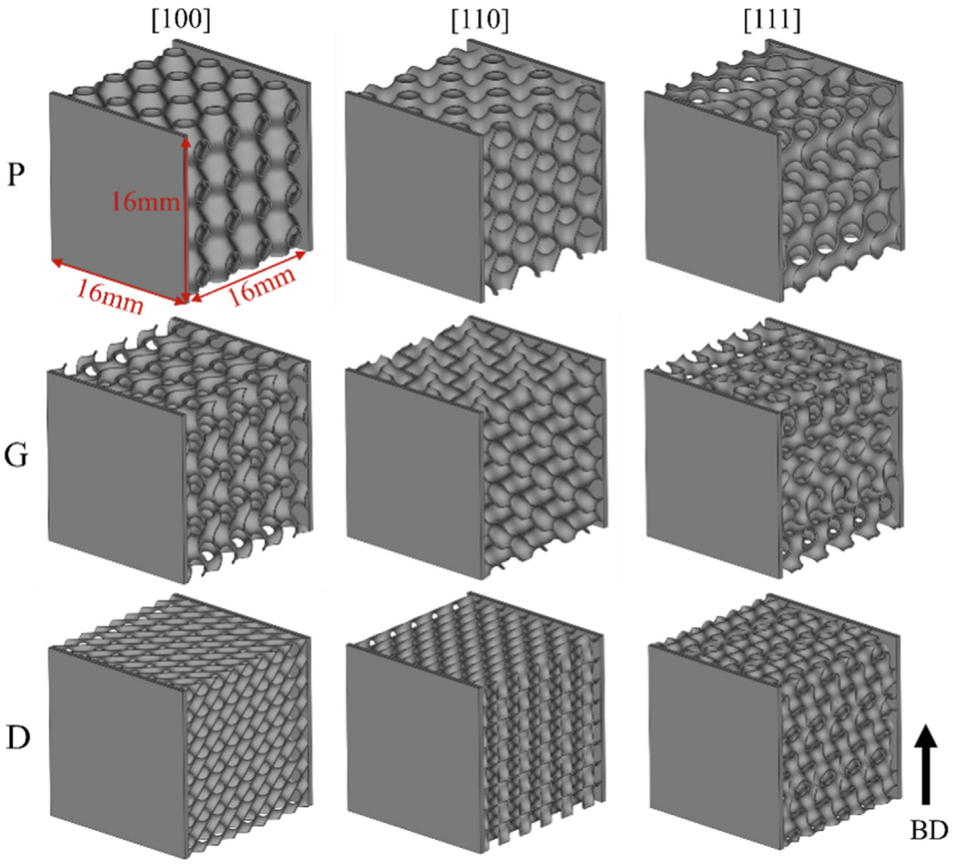

Fig. 1. 3D models of TPMS shell lattices with 10% relative density and different types and orientations for μLPBF.

with different shell thickness and cell orientations. Two end plates with a thickness of 0.5 mm are added with in-plane direction parallel to the building direction, as shown in Fig. 1. The addition of end plates keeps consistent with the previous work [6], which allows direct comparison of mechanical response of the TPMS structures fabricated by micro and conventional LPBF as discussed in following sections. In addition, the possible overhangs at the edge of the sample can be avoided to guarantee successful fabrication. During compression test, the two parallel plates also ensure full contact with the loading plate, which can provide more accurate deformation data. Moreover, extra experiments prove that the end plates have limited influence on the mechanical behavior of the TPMS structures, as shown in Fig. 2 (d), in which the TPMS structures ($\bar{\rho}$ about 5 %) with/without end plates show similar stress–strain curves and same deformation pattern at same strain. Details of the TPMS structures for μLPBF can be found in Table 1. In this work, the specimens are named according to the relative density pre-defined in STL models. For instance, P100_r5 denotes P-type structure with [1 0 0] direction along the loading direction and with predefined $\bar{\rho}$ 5 %.

TPMS structures were fabricated by a customized μLPBF system (Hans' Laser M100μ), which is equipped with a continuous 500 W IPG fiber laser (λ = 1.07 μm) with beam spot size of 25 μm. By using this μLPBF system, light-weight thin-wall TPMS structure with low relative density of about 6.77 % can be realized (Table 1). Austenitic SS316L powder with particle size of 5 ~25 μm (D50 = 16.27 μm) produced by gas atomization technology was used for fabrication. The adopted processing parameters are listed in Table 2.

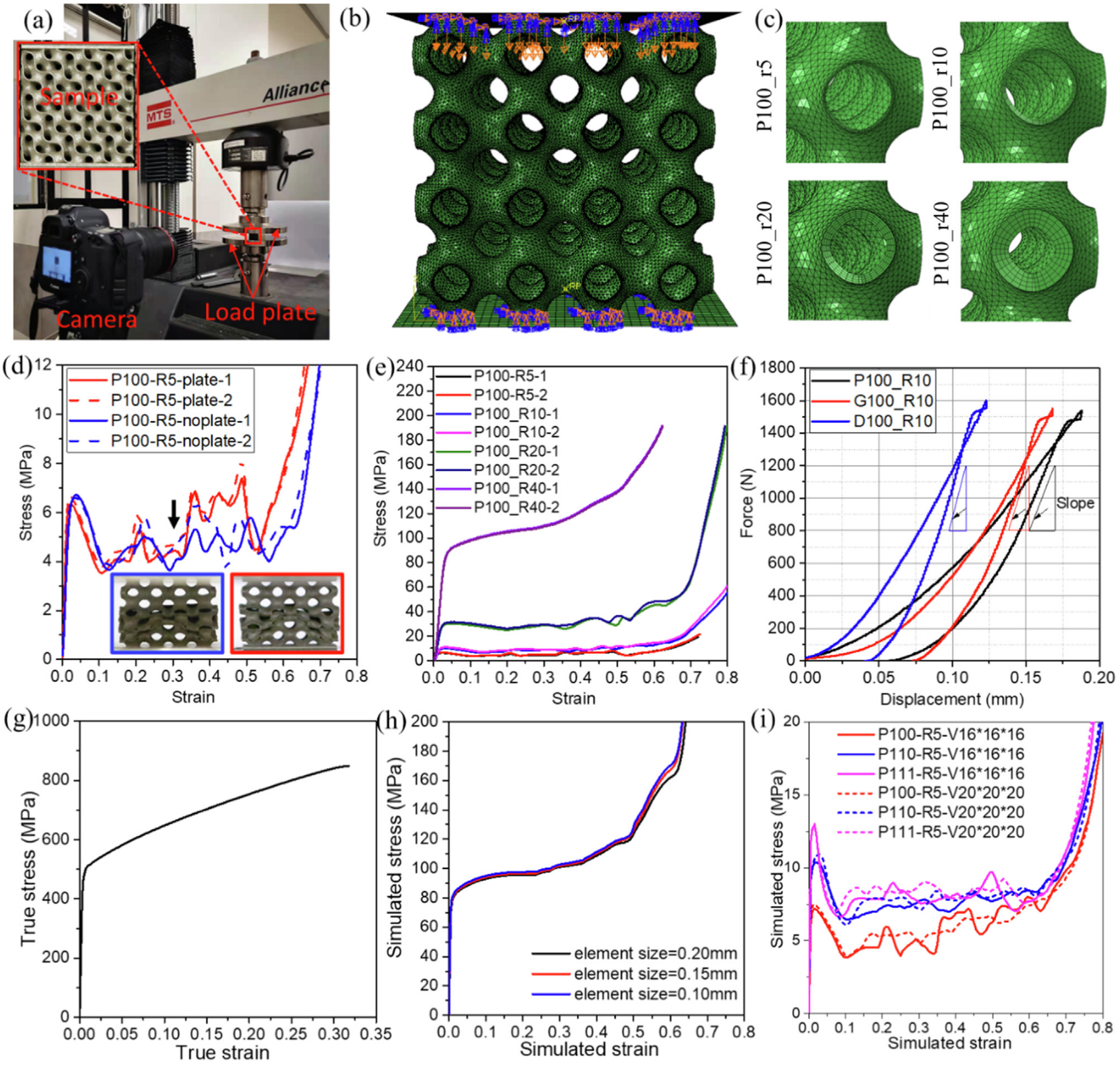

Fig. 2. Experimental and FE modeling configurations: (a) setup of compression tests; (b) assembly of P100_r5 FE model; (c) representative unit cells of P100 FE models with four elements through shell thickness; (d) experimental stress–strain behavior of the P100_r5 with and without end plates; (e) the repeatability of the stress–strain curves of the as-printed TPMS structures; (f) the loading–unloading curves for measuring modulus of TPMS structures; (g) the true stress-plastic strain curve of 316L stainless steel produced by μLPBF; (h) numerical stress–strain behavior of the P100_r40 meshed with different element sizes; (i) numerical stress–strain behavior of various P-type TPMS with different sample sizes.

Table 1
Features of the TPMS structures fabricated by μLPBF.

TPMS type	STL $\bar{\rho}$ (%)	STL t (mm)	Measured $\bar{\rho}$ (%)	Measured t (mm)	Nominal t (mm)	Effective t (mm)	Effective $\bar{\rho}$ (%)
P100	5/10/20/40	0.085/0.170 0.339/0.678	6.77/9.36/18.7/36.4	0.141/0.181/0.341/0.650	0.113/0.158/0.312/0.619	0.085/0.128/0.282/0.589	5.01/7.55/16.64/34.75
G100	5/10/20/40	0.065/0.129 0.258/0.516	8.07/11.2/19.0/36.5	0.117/0.163/0.252/0.538	0.103/0.145/0.245/0.468	0.073/0.115/0.215/0.438	5.67/8.93/16.70/34.01
D100	10/20/40	0.104/0.208 0.416	12.10/20.06/37.57	0.137/0.205/0.423	0.125/0.207/0.385	0.080/0.162/0.340	7.68/15.55/32.63
P110/P111	10/10	0.167/0.167	10.50/10.44	0.201/0.199	0.179/0.177	0.149/0.147	8.93/8.81
G110/G111	10/10	0.130/0.130	11.19/11.31	0.164/0.167	0.145/0.147	0.115/0.117	8.85/9.07
D110/D111	10/10	0.104/0.104	11.88/11.90	0.137/0.141	0.124/0.128	0.079/0.083	7.61/7.96

2.2. Sample characterization

All the samples were cut by Electrical Discharge Machining (EDM) from the substrate, followed by ultrasonic cleaning to remove the adhered loose powders and oil. The surface morphology and shell thickness of TPMS structures were observed and measured using scanning electron microscope (SEM) JCM-6000 PLUS. Dry weighing method was used to measure the relative density of the as-printed TPMS structures. The weight of TPMS cores m_{TPMS} was calculated excluding the weight of end plates. The dimensions (length × width × height) were measured to evaluate the cubic volume V_{cube} which the TPMS structure occupies. Then, the measured relative density $\bar{\rho}$ can be expressed as.

$$\bar{\rho} = \frac{m_{TPMS}}{\rho_s \cdot V_{cube}} \tag{3}$$

where ρ_s is the density of solid material. Since the middle surface area of the TPMS cores A_{surf} is difficult to be measured, it was extracted from 3D STL models as an approximation of the actual surface area. The nominal thickness t can be calculated according to the measured relative density and surface area (Equation (4)). It should be noted the nominal thickness is calculated without excluding the effect of adhered partially melted powders, which have no contribution to the mechanical performance or even serve as detrimental origins.

$$t_{nominal} = \frac{V_{cube} \cdot \bar{\rho}}{A_{surf}} \tag{4}$$

2.3. Quasi-static compression tests

Quasi-static compression tests of TPMS shell lattices with different shell thickness and loading orientations were conducted on an MTS universal test machine at a rate of 0.96 mm/min and stopped after densification, following the standard ISO 13314:2011 [35]. The loading direction is perpendicular to the end plate as well as the building direction. A camera was used for capturing the deformation modes of the TPMS structures (Fig. 2 (a)). The stress was calculated as the force divided by the area of the cubic cross section, and the strain was defined as displacement of the crosshead divided by the height of TPMS cores. Since the mechanical behavior of the as-printed specimens presents desirable repeatability, as shown in Fig. 2 (e), two specimens of each type of structures were tested, which was also adopted in other studies [29,33,36,37]. For measurement of the elastic property, for example, Young's modulus, Ashby et al. [38] suggested that the modulus of the cellular structures calculated from the loading elastic stage could be unrepresentative due to localized plasticity. Instead, it is recommended to calculate the Young's modulus from the unloading curve, as shown in Fig. 2 (f). To this end, three loading–unloading tests for each type of structures were conducted, in which all samples were loaded to 1500 N and unloaded at a constant crosshead speed of 0.1 mm/min. Besides, the stiffness of the machine should be considered as well, whose influence should be removed to calculate the Young's modulus of TPMS cores [22].

Table 2
Process parameter configurations.

Parameters	Value
Laser power	50 W
Laser spot size	25 μm
Layer thickness	10 μm
Scanning speed	1000 mm/s
Hatch spacing	50 μm
Hatch angle	67°

2.4. Finite element modelling

Finite element (FE) modelling was conducted to simulate the compressive behavior of the TPMS shell lattices. Since the post yield deformation is quite non-periodic, full scale model is required to accurately capture the deformation mode and stress localization [6]. The compressive responses of the G-, D-, P-type TPMS are analysed using FE package Abaqus/Explicit 2017. Fig. 2 (b) shows the assembly of FE models of TPMS structures. Two rigid plates are modelled and tied to the top and bottom nodes of the TPMS structure, which ensures the same boundary conditions as the printed TPMS samples. All degrees-of-freedom of the bottom plate are fixed, and the top plate is moved down with a strain rate of 10^{-3} s^{-1}. General hard contact is assigned for the assembly. Semi-automatic mass scaling was applied with a minimum target time increment of 5×10^{-4} s, which can ensure a low ratio of kinetic energy to internal energy (<10 %) during compression. The TPMS shell lattices are meshed with 3D linear triangular prism elements (C3D6) with an average element size of 0.2 mm. The meshing with C3D6 is realized by offsetting the STL surface mesh to a certain value with four elements through thickness (Fig. 2 (c)). The tensile property of SS316L produced using the same process parameters for TPMS, as reported in previous work [21], is used for FE modelling with isotropic hardening [6]. The true stress–strain curve of the base material is shown in Fig. 2 (g). The Young's modulus and Poisson's ratio are set to be 190GPa and 0.3, respectively. No failure model is used since the sheet fracture is not evident in the experiment after the onset of densification [6]. The mesh sensitivity of FE models was studied, as shown in Fig. 2 (h). Compared with 0.1 and 0.15 mm, the element size of 0.2 mm can not only have similar FE results but also save computation costs. Fig. 2 (i) proves that the selected sample size of 16 × 16 × 16 mm^3 was representative as it provides almost the same stress–strain results to the volume of $20 \times 20 \times 20\ \mathrm{mm}^3$.

Since the nominal thickness includes the effect of adhered powders, which have no contribution to mechanical property, the use of nominal thickness in FE models would result in overestimated mechanical properties. Therefore, there exists an effective thickness for FE model that can predict the mechanical properties more accurately with the effect of adhered powder excluded. The effective thicknesses of the various TPMS structures for FE modelling are listed in Table 1, where $t_{effective} = t_{nominal} - t_{reduction}$. Previous work indicated that the thickness reduction method can obtain a desired agreement between experimental and numerical results [6]. In this work, empiric thickness reduction values of 30 μm for P- and G-type structures and 45 μm for D-type ones were determined to achieve the best fit of experimental results, with which the underlying mechanisms of mechanical response in terms of mechanical properties and deformation mode of TPMS structures can be accurately understood. It should be noted that the thickness reduction value used in this work is not twice of the powder size which was adopted in [6]. Although it is not directly determined by powder size, the thickness reduction value does have correlation with the latter. The thickness reduction values for our μLPBFed TPMS are smaller than that (60 μm) for conventional LPBFed TPMS [6], which is associated with the smaller powder size used in μLPBF. In addition, the slightly higher thickness reduction for D-type structures results from its higher surface area, which capture more attached powders on the surface during printing. Thus, the nominal thickness of D-type structures involves more volume contribution from the adhered powder, which should be excluded. However, using an empiric thickness reduction value is a limitation, which is not applicable to strut-based lattice structures. Therefore, in future work, high-resolution geometry reconstruction and physics-based constitutive model considering the adhered powders and internal defects should be established to predict the mechanical response of lattice structures fabricated by LPBF.

3. Results and discussion

3.1. Manufacturability of TPMS shell lattices by μLPBF

Fig. 3 shows the as-printed low-density G-, D- and P-type TPMS structures with [1 0 0] direction, and the surface quality was examined by SEM imaging. Both top and side surfaces are adhered with a layer of partially melted powders, which is more significant for the side surface. Since the side surface is exposed to the powder sink, more powders can be attracted to the end of the track and partially melted, leading to a higher surface roughness than top surface. Moreover, aggregated powder is observed on the downward surfaces, which is a common phenomenon in LPBF process [6]. On the other hand, according to our previous study [21], the top surface roughness *Ra* is 3.40 μm for μLPBF, respectively, smaller than those prepared by conventional LPBF. This advantage comes from the finer powder and fine laser beam used in μLPBF system, with which lightweight TPMS structures with thinner shell thickness and higher fidelity can be readily produced.

The relative density of the as-printed TPMS specimens is measured, as shown in Table 1. The discrepancy in the designed and measured relative density is mainly from the surface-attached powders, the inaccuracy of the shell thickness after printing, and the possible internal defects [39]. For the adhered powders, they are inevitable in powder-based AM technology [12]. Even post treatment, such as chemical etching, cannot fully remove these powders. The adhered powders increase the measured relative

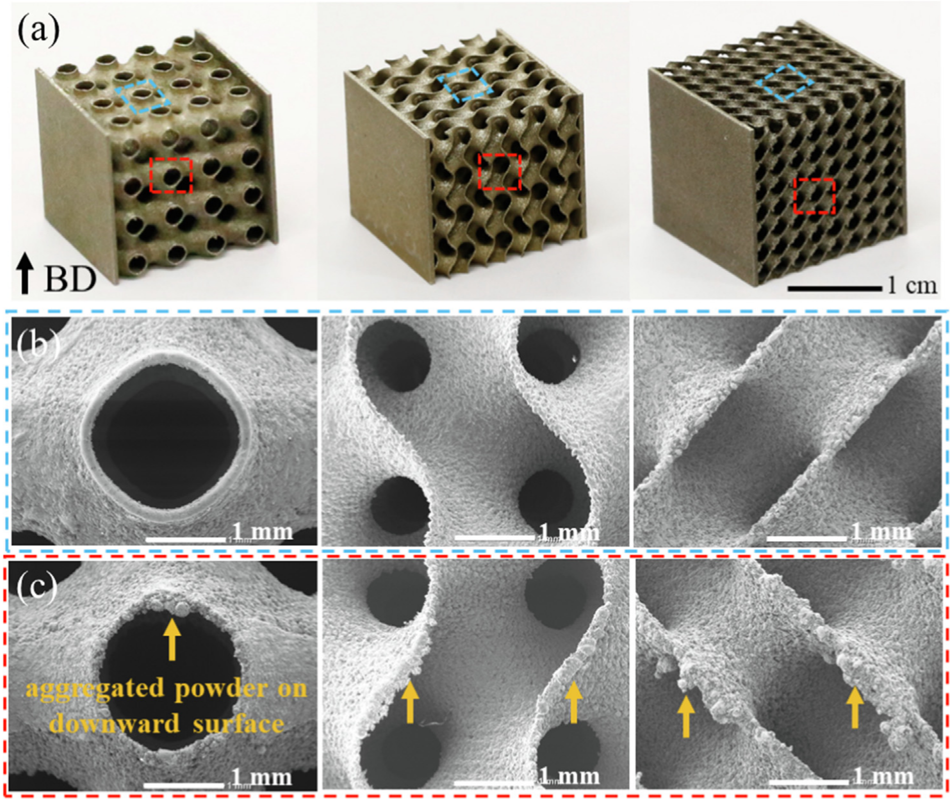

Fig. 3. Characterization of surface morphology of the low-density TPMS structures: (a) as-printed P100_r5, G100_r5, and D100_r10 structures; (b) SEM observations of selected top surfaces (blue); (c) SEM observations of selected side surfaces (red). (For interpretation of the references to colour in this figure legend, the reader is referred to the web version of this article.)

density, but make no positive contribution to the mechanical stiffness and strength and even initiate fatigue cracks for lattices made of brittle metals and alloys [40]. The internal defects such as pores and cracks could lead to reduced relative density and thereby deteriorate the mechanical properties. Table 1 also shows the measured shell thickness of as-printed TPMS structures, which is slightly larger than the nominal thickness. Generally, the deviation of the shell thickness after printing comes from the molten pool dimension and the toolpath planning for μLPBF. In this work, the μLPBF can ensure better geometry accuracy compared with conventional LPBF due to the smaller molten pool. Despite of this, there is still inevitable deviation between the designed and measured shell thickness, which is more significant for low relative density TPMS structures.

3.2. Stress–strain curves

Fig. 4 presents the experimental and numerical compressive stress–strain curves of G-, D- and P-type TPMS structures with different shell thicknesses and cell orientations. The comparison of experimental and simulated curves demonstrates a good agreement, indicating that the FE models and the proposed thickness reduction method are effective in predicting the deformation mechanism and the mechanical properties of the structures. Specifically, low-density (5 % and 10 %) TPMS structures are slightly overestimated by FE models, while high-density (40 %) ones are marginally underestimated, and the TPMS structures with nominal relative density of 20 % suggest the best agreement between experimental and numerical curves. This could be explained by the possibility that the adhered powder layer plays a more important role for low-density structures than the moderate-density ones.

In general, the experimental and predicted stress–strain responses present three typical deformation stages of cellular structures, i.e., linear elastic deformation region, and stress plateau region followed by densification region. After elastic deformation, plateau region begins where the cells collapse due to buckling, brittle fracture or yield depending on the properties of base materials and unit cell structures [41]. According to previous literature, bending-dominated lattice structures usually present almost constant stress during plateau region, while stretching-dominated structures illustrate a stress fluctuation [42]. It should be noted that there is no brittle fracture due to the high strength – ductility combination of the material SS316L produced by LPBF [43]. The densification of the structures refers to that all the components (shells) begin to fully contact with each other, resulting in a sharp increase of stress. From Fig. 4, we can conclude that the stress–strain response especially of plateau region highly depend on the

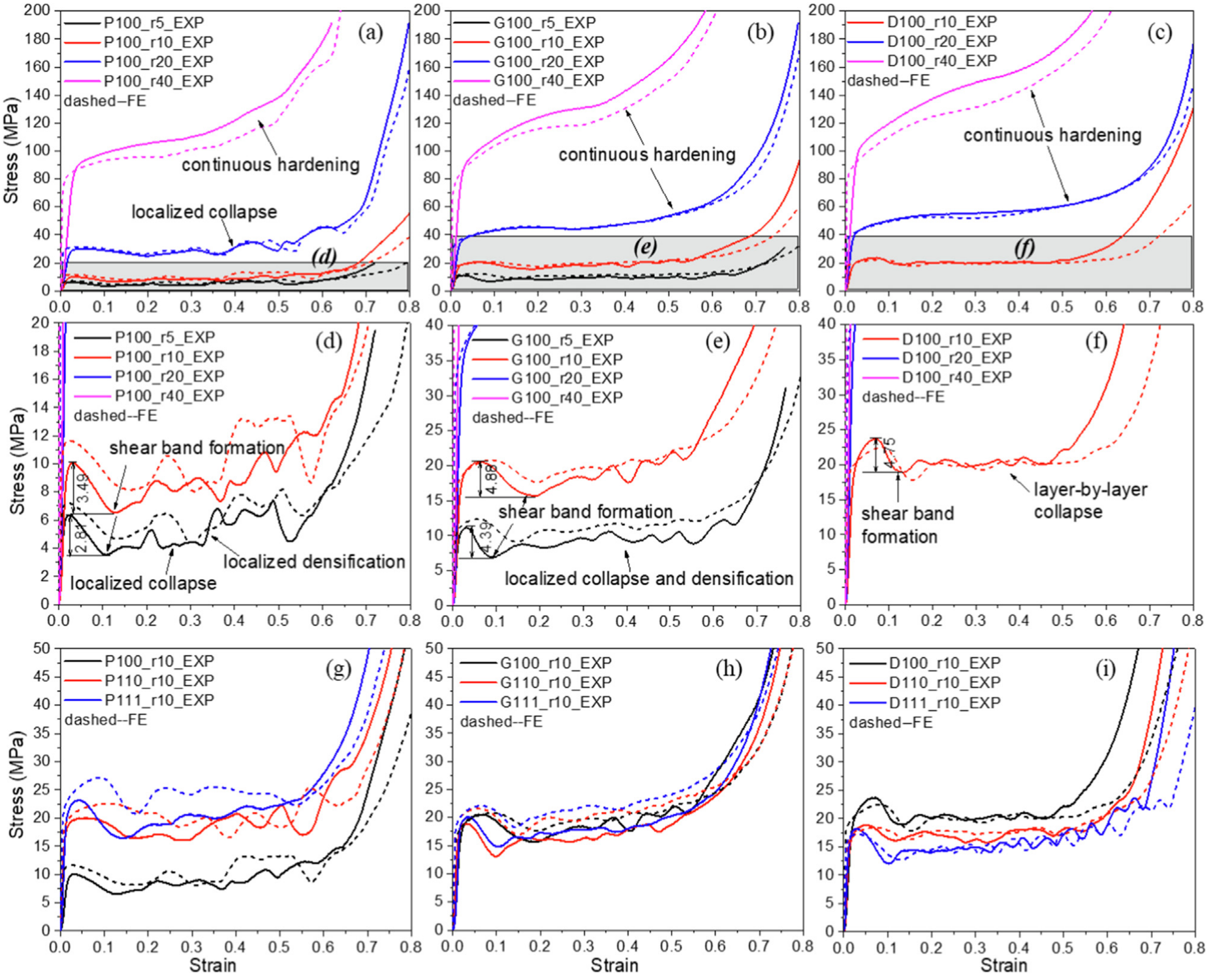

Fig. 4. Experimental and numerical compressive stress–strain curves of G-, D- and P-type TPMS structures with different shell thickness and cell orientations; (d, e and f) are the corresponding zoom-in sections of (a, b and c); the term EXP denotes experimental results and FE denotes the finite element simulation results.

TPMS geometry, the shell thickness (relative density) and the cell orientation.

For TPMS structures with smaller shell thicknesses (relative density lower than 10 %), all samples display an initial peak stress followed by the significant stress drop and this stress drop is associated with shear band formation. As shown in Fig. 4 (d, e, f), which are the corresponding zoom-in sections of Fig. 4 (a, b, c), the reduction of initial peak stress and corresponding strain increases with increasing shell thickness. In addition, P-type structure has smaller reduction of initial peak stress compared with G- and D-type TPMS structures. Subsequently, significant stress fluctuation was found to dominate the plastic deformation region before the onset of densification in low-density TPMS structures. Among the three types of TPMS, G-type structure shows the least stress fluctuations and relatively stable stress–strain behavior, while P-type shows intensive stress fluctuation associated with localized plastic deformation and collapse of the curved walls during plateau region. This geometry-dependent difference can be explained by the internal material distribution, which affects the failure behavior and load-bearing capacity of the structure [27,44]. In detail, Zhao et al. [27] reported that the stress evolution during compression of TPMS structures is highly corelated with the material distribution along loading direction. Downing et al. [44] even improved the mechanical properties of TPMS structures by tailoring the localized material distribution. Therefore, the internal material distribution is an important factor, which affects the mechanical properties of TPMS structures. The internal material distribution can be simplified as the cross-section area of TPMS structures perpendicular to the loading direction as a function of height of TPMS cores, as shown in Fig. 5 (a, b, c). Obviously, the internal material distribution of P100 structure is relatively heterogeneous, while those of G100 and D100 structure suggest a smaller variation along loading direction. Thus, the load-bearing capacity along loading direction is much more non-uniform for P100 structure, leading to unstable fluctuating region [27]. With increasing shell thickness, the initial peak stress, significant initial softening effect and stress fluctuation gradually disappear. Instead, a smooth plateau stress–strain curve (e.g., G100_r20 and D100_r20) or a continuous hardening response associated with bulk deformation in all of the TPMS structures with 40 % predefined relative density are observed, as shown in Fig. 4 (a, b, c).

Fig. 4 (g, h, i) show the compressive stress–strain response of G-, D- and P-type TPMS structures with a predefined relative density of 10 % compressed along three different loading orientations, namely, [1 0 0], [1 1 0] and [1 1 1]. Specifically, P-type TPMS structures with different cell orientations demonstrate distinct stress–strain responses and varied plateau stress levels, indicating a significant anisotropy of compressive properties. In contrast, G-type lattices present a near-isotropic behavior with plateau stress of ~18 MPa. It can also be explained according to the internal material distribution (Fig. 5 (a, b, c)). For P-type structure, the distribution of cross-section area along loading direction, especially the amplitude, is significantly different for the three different orientations. In comparison, the variation of cell orientation does not notably change the distribution of internal material for G-type structure as shown in Fig. 5 (a, b, c), which leads to a more isotropic load-bearing capability and deformation behavior.

3.3. Compressive deformation mechanism

Deformation histories (i.e., the evolution of deformation as well as stress distributions) simulated by FE models are compared with experimental ones to better understand the deformation mechanism, as shown in Figs. 6–8, as well as in the supplementary videos. The deformation patterns at different strains as described by experiments and FE models are consistent, further validating the FE modeling method. This section focuses on the effect of shell thicknesses, loading orientations and TPMS types on the deformation mechanism of TPMS structures through combined experimental and numerical results.

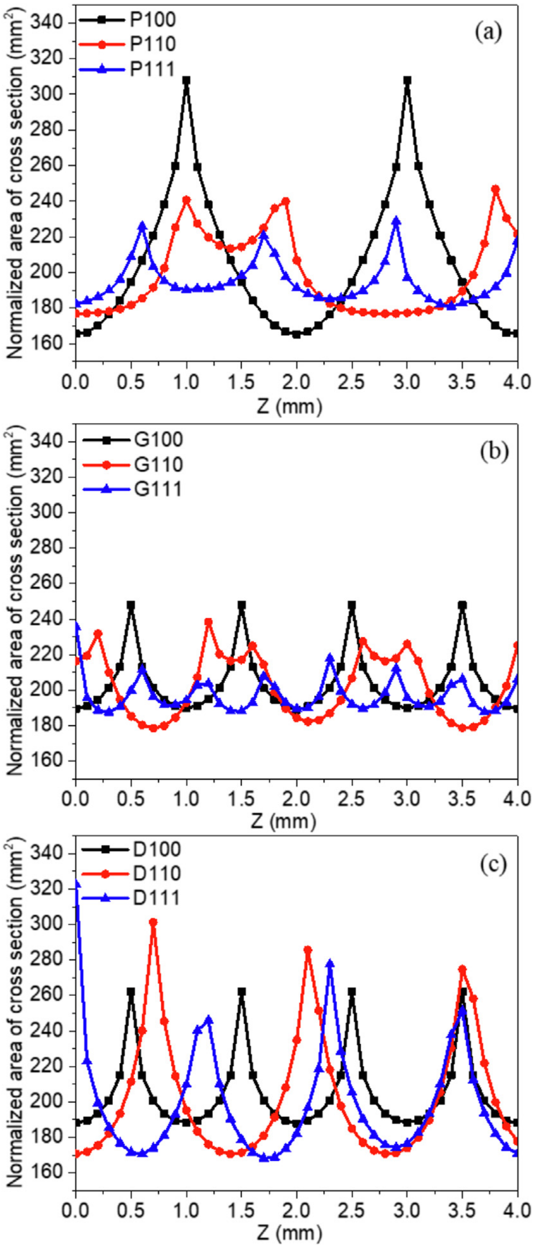

Fig. 5. The distribution of cross-section area normalized by effective $\bar{\rho}$ of (a) P-type, (b) G-type and (c) D-type TPMS structures; the cross-section area was calculated as perimeter of slice contour multiplying effective thickness corresponding to TPMS structures with predefined $\bar{\rho}$ of 10 %.

It is found that the change of shell thickness for all of the G-, D- and P-types of TPMS structures leads to a transition of deformation mechanism. In general, for small shell thicknesses, the internal stress is non-uniformly distributed within the structure, representing localized deformation and collapse; with shell thickness increasing, the stress distribution becomes more uniform. The deformation mode transforms from localized plastic collapse with significant stress fluctuation to bulk deformation behavior with continuous hardening effect. Therefore, there exists a threshold of predefined relative density for the G-, D- and P-types of TPMS structures, above which the deformation mechanism transforms

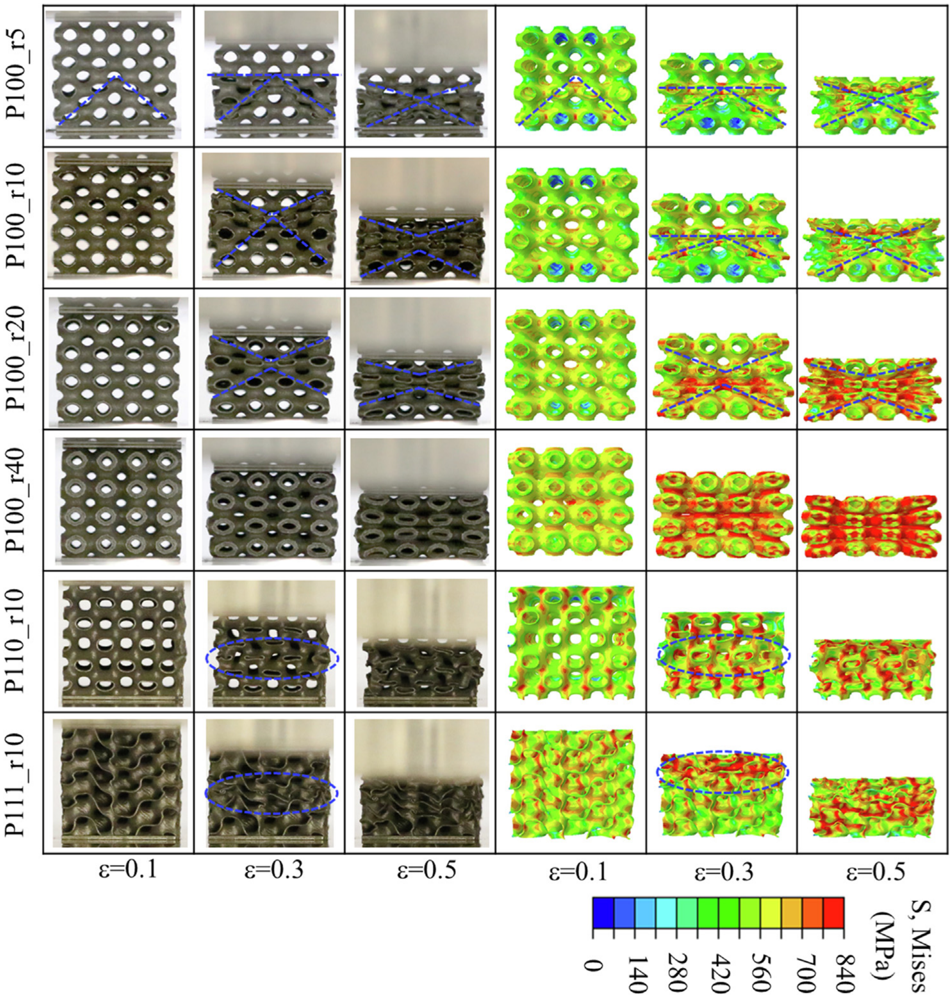

Fig. 6. Experimental and numerical results of deformation behaviors of P-type TPMS shell lattices with different shell thickness and cell orientations; three strain levels of 0.1, 0.3 and 0.5 were selected for illustration.

from localized mode to bulk deformation mode. It is noted that the threshold for P-type structure is relatively higher (predefined $\bar{\rho}$ over 20 %) than those for G- and D-type ones (predefined $\bar{\rho}$ below 20 %). This is because the unique P100-type structure has significant non-uniform internal material distribution (Fig. 5 (a)), leading to heterogenous load-bearing capacity and a resultant localized deformation mode.

With particular interest in low relative density structures, by comparing the stress–strain curve (Fig. 4) and the deformation history recorded by experiments and FE modelling (supplementary videos), it is found that the significant post-yield stress drop is associated with the formation of shear band that two neighboring areas separating and sliding at an approximate strain 0.1 or 0.15, which is consistent with that reported in [27]. Similar shear failure was also observed in strut-based lattice structures [45,46], where shear band usually occurs with an angle of 45° to the loading direction. For the deformation mode right after the initial peak stress, it is found that the post-yield periodic or non-periodic stress drop and recovery in low-density TPMS structures correspond to localized plastic collapse and localized densification of the curved walls, respectively. Specifically, P-type structure at lower relative density deforms and collapses by diagonal shear, displaying double shear bands, as shown in Fig. 6 (P100_r5, r10 and r20). The failure by diagonal shear leads to significant heterogeneous stress distribution during the plateau region. For G-type TPMS lattices of lower relative density, the crushing behavior is heterogeneous and concentrated at the central layers before densification, as shown in Fig. 7 (G100_r5 and r10). For D-type TPMS lattices, it is interesting to see that the structure with the smallest thickness shows a distinct layer-by-layer crushing behavior (Fig. 8, D100_r10), where each layer collapse corresponds to one stress peak and valley on the stress–strain curve during plateau region. On the other hand, with increasing shell thickness (relative density), the initial peak stress and the stress drop gradually disappear (Fig. 4 (d, e)), which suggests that the shearing behavior is gradually inhibited in high relative density structures. Instead, the unit cells as a whole tend to deform uniformly due to plastic yield instead of localized collapse. Our findings highlight that the failure behavior and deformation mechanism of TPMS shell lattices change from bulk deformation in moderate relative densities (20–40 %) to localized shear bands or layer crushing behavior in low relative densities (<10 %), which are not reported in previous studies due to SLM printing limitations.

The anisotropy of compressive deformation behavior is found to be dependent on the type of TPMS structures (see Figs. 6-8 and supplementary videos). In detail, P100 structure presents a lower compressive plateau stress compared with the other two orientations (Fig. 4 (g)). As reflected in the deformation mode, P100 structures exhibit localized formation of diagonal double shear bands due to its lower load-bearing capability. In contrast, P110 and

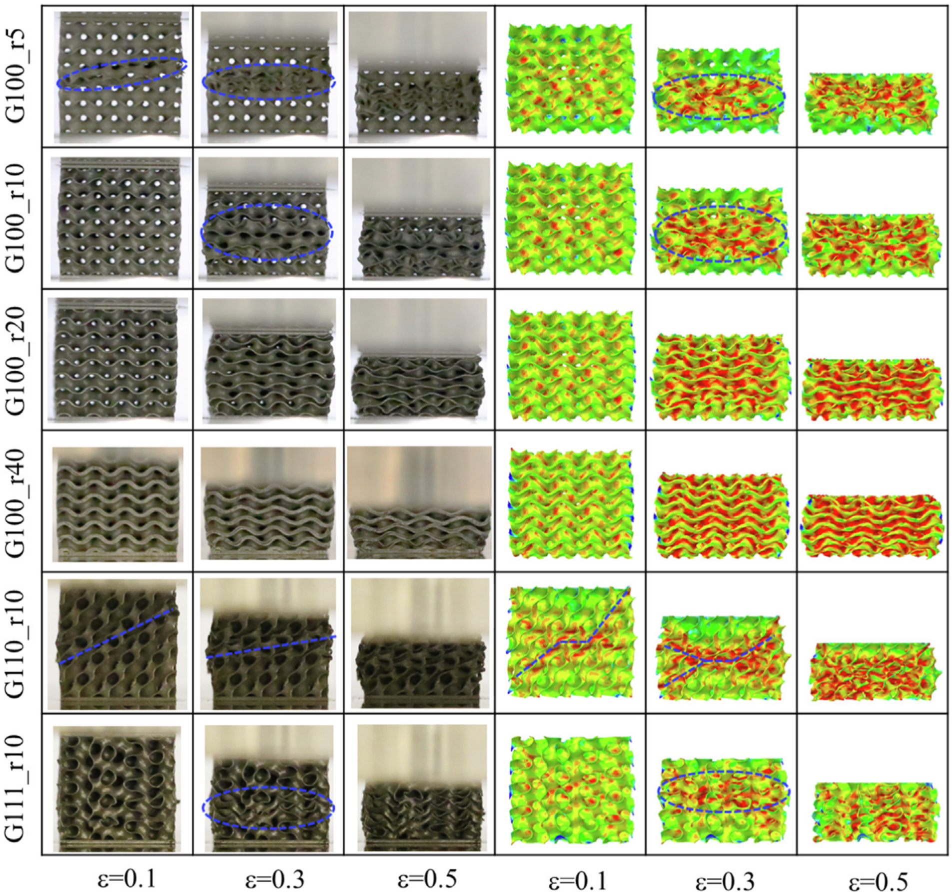

Fig. 7. Experimental and numerical results of deformation behaviors of G-type TPMS shell lattices with different shell thickness and cell orientations; three strain levels of 0.1, 0.3 and 0.5 were selected for illustration; legend for FE result is same as that in Fig. 6.

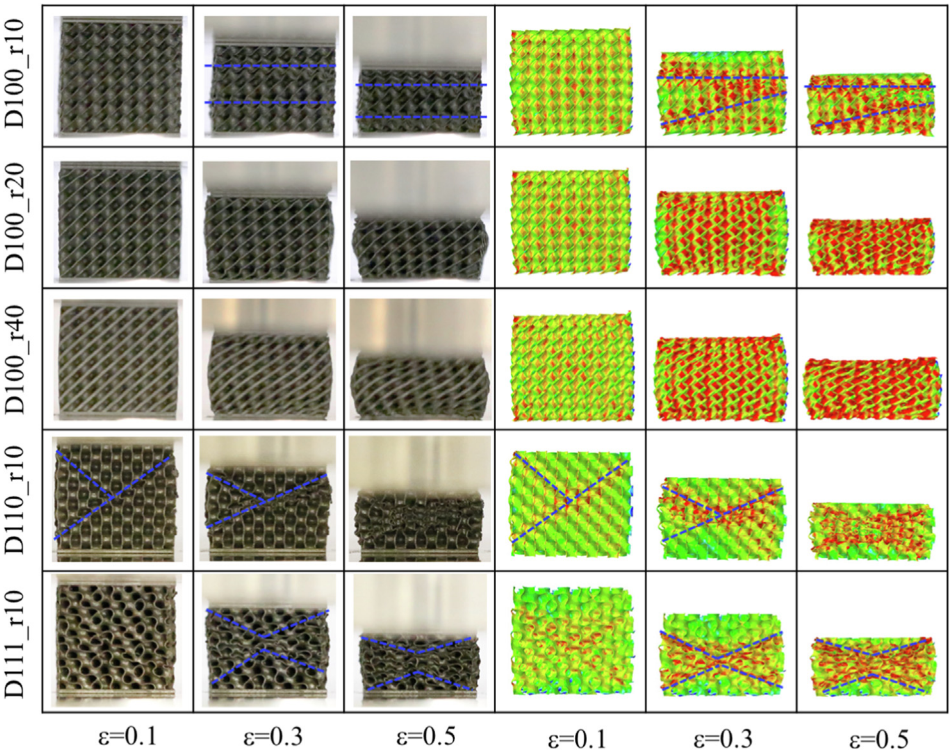

Fig. 8. Experimental and numerical results of deformation behaviors of D-type TPMS shell lattices with different shell thickness and cell orientations; three strain levels of 0.1, 0.3 and 0.5 were selected for illustration; legend for FE result is same as that in Fig. 6.

P111 structures locally deform with a horizonal shear band firstly formed approximately in the central layers of TPMS cores, followed by layer-by-layer collapse. For G-type TPMS, the [1 1 0] orientation produces a tilted shear band, while the [1 0 0] and [1 1 1] orientations experience layer-by-layer failure of horizontal layers. For D-type TPMS, D100 structure deforms in a clear lay-by-layer mode, while double shear bands are developed in the structures with [1 1 0] and [1 1 1] orientations.

3.4. Effect of TPMS geometry on mechanical properties

The mechanical properties of these TPMS shell lattices including Young's modulus, plateau stress, densification strain and energy absorption are extracted from the stress–strain curves. Especially, the determination of Young's modulus is based on unloading stress–strain curve as is mentioned in Section 2.3. Since there is no initial peak stress in some cases of high-density TPMS structures, the plateau stress is selected as the strength indicator, which is determined as the mean stress within the strain range of 0.2–0.4 [35]. In this work, the energy absorption capability is described by the mechanical work performed (per unit volume) when uniaxially deforming the TPMS structures to the onset strain of densification [35]. The absorbed energy can be expressed as:

$$W = \int_0^{\varepsilon_D} \sigma(\varepsilon) d\varepsilon \tag{5}$$

where ε_D denotes the onset strain of densification. It is calculated as the strain at which energy absorption efficiency reaches a maximum (the last local maximum of the efficiency curve is used in this work) [47]. Table 3 lists the experimental and predicted densification strains, and the overall maximum error is 16.99 %. The energy absorption efficiency η is expressed as:

$$\eta = \frac{1}{\sigma(\varepsilon)} \int_0^{\varepsilon} \sigma(\varepsilon) d\varepsilon \tag{6}$$

Fig. 9 (a, b, c) show the normalized mechanical properties of the TPMS shell lattices with different cell types and orientations. Generally, the FE predicted mechanical properties are slightly higher than the experimental ones. The effect of cell orientation on mechanical properties is different for different TPMS types. The anisotropy ratio of stiffness R_E, plateau strength R_σ and energy absorption capability R_W can be quantified as:

$$R_E = \frac{\max(E_{[100],[110],[111]})}{\min(E_{[100],[110],[111]})}, R_\sigma = \frac{\max(\sigma_{pl[100],[110],[111]})}{\min(\sigma_{pl[100],[110],[111]})},$$
$$R_W = \frac{\max(W_{[100],[110],[111]})}{\min(W_{[100],[110],[111]})} \tag{7}$$

where E, σ_{pl} and W are experimental values of stiffness, plateau strength and absorbed energy of TPMS structures with different orientations. For samples with 10 % relative density, the calculated values of R_E, R_σ and R_W are 1.54, 2.04 and 1.81 for P-type TPMS, 1.11, 1.10 and 1.04 for G-type TPMS, 1.22, 1.42 and 1.13 for D-type TPMS, respectively. P-type structures show the highest anisotropy of properties, while G-type structures with [1 0 0], [1 1 0] and [1 1 1] orientations provide similar level of stiffness, plateau strength and energy absorption capability.

Table 3
Experimental and predicted densification strains.

Structure	Orientation	Effective $\bar{\rho}$ (%)	Ave. ε_D, measured	ε_D, FE	Error (%)
P	100	5.01	0.530	0.635	16.53
	100	7.55	0.645	0.575	12.17
	100	16.64	0.632	0.650	2.77
	100	34.75	0.515	0.615	16.26
	110	8.93	0.663	0.640	3.59
	111	8.81	0.548	0.550	0.36
G	100	5.67	0.651	0.570	14.21
	100	8.93	0.539	0.620	13.06
	100	16.7	0.580	0.630	7.94
	100	34.01	0.567	0.540	5.00
	110	8.85	0.563	0.615	8.46
	111	9.07	0.549	0.590	6.95
D	100	7.68	0.518	0.610	15.08
	100	15.55	0.613	0.630	2.70
	100	32.63	0.563	0.585	3.76
	110	7.61	0.552	0.665	16.99
	111	7.96	0.685	0.740	7.43

Among the nine types of structures, D100 structure provides the best combination of stiffness, plateau strength and energy absorption, while P100 structure has the lowest properties. Although P110 structure has a relatively lower plateau strength, it absorbs the highest energy during compressive experiments, due to its large onset strain of densification strain of 0.663, as shown in Table 3. The comprehensive mechanical properties of P110 and P111 structures are slightly higher than those of all the different oriented G-type structures and comparable to D110 and D111 structures. Moreover, it is found that the plateau strength is related to the minimum value of the horizontal cross-section area, namely, the minimum material for load bearing. As shown in Fig. 5 (a, b, c), the sequences of the minimum value of cross-section area for P-, G- and D-type structures are: P111 > P110 > P100, G100 > G111 > G110, and D100 > D110 > D111, respectively. The same sequences are agreed for the plateau strength of P-, G- and D-type structures with different orientations, as shown in Fig. 9 (b).

3.5. Light-weighting potential of SS316L TPMS fabricated by μLPBF

The light-weighting potential of TPMS lattices is associated with the scaling of mechanical properties (stiffness, strength and energy absorption capability) as a function of relative density. For a TPMS structure with good light-weighting potential, the mechanical properties should not scale down too fast with the decrease of relative density. The slower the property decrease with relative density, the better the light-weighting potential. In this case, power law fitting of the mechanical properties as a function of effective relative density (shell thickness) is used to describe the scaling behavior of the mechanical properties of these as-printed TPMS shell lattices [6]. Based on the theoretical work by Gibson and Ashby [48], normalized Young's modulus E, plateau stress σ_{pl} and absorbed energy W are utilized to compare and analyze the compressive properties of the TPMS structures, which are expressed as:

$$\frac{E}{E_S} = C_1 * \bar{\rho}^{n_1}, \frac{\sigma_{pl}}{\sigma_y} = C_2 * \bar{\rho}^{n_2}, \frac{W}{\sigma_y} = C_3 * \bar{\rho}^{n_3} \tag{8}$$

where E_S and σ_y are Young's modulus and yield strength of the bulk SS316L parts produced by μLPBF. The coefficients C_1, C_2, C_3 and exponents n_1, n_2, n_3 differ for different TPMS geometries. Apparently, the smaller the exponents, the better the light-weighting potential. Fig. 9 (d, e, f) show the positive power relationship between the normalized compressive properties and effective relative density, as well as the fitted equations. The values of R^2 for all fitted curves (both experimental and numerical ones) are within the range of 0.980–0.990. In general, the fitted exponents (n_1, n_2, n_3) of numerical results are slightly smaller than those of experimental results for all the G-, D- and P-type structures, which indicate that the practical mechanical properties of the as-printed structures deteriorate faster with decreasing relative density than the FE predicted ones. This can be attributed to the structural defects such as

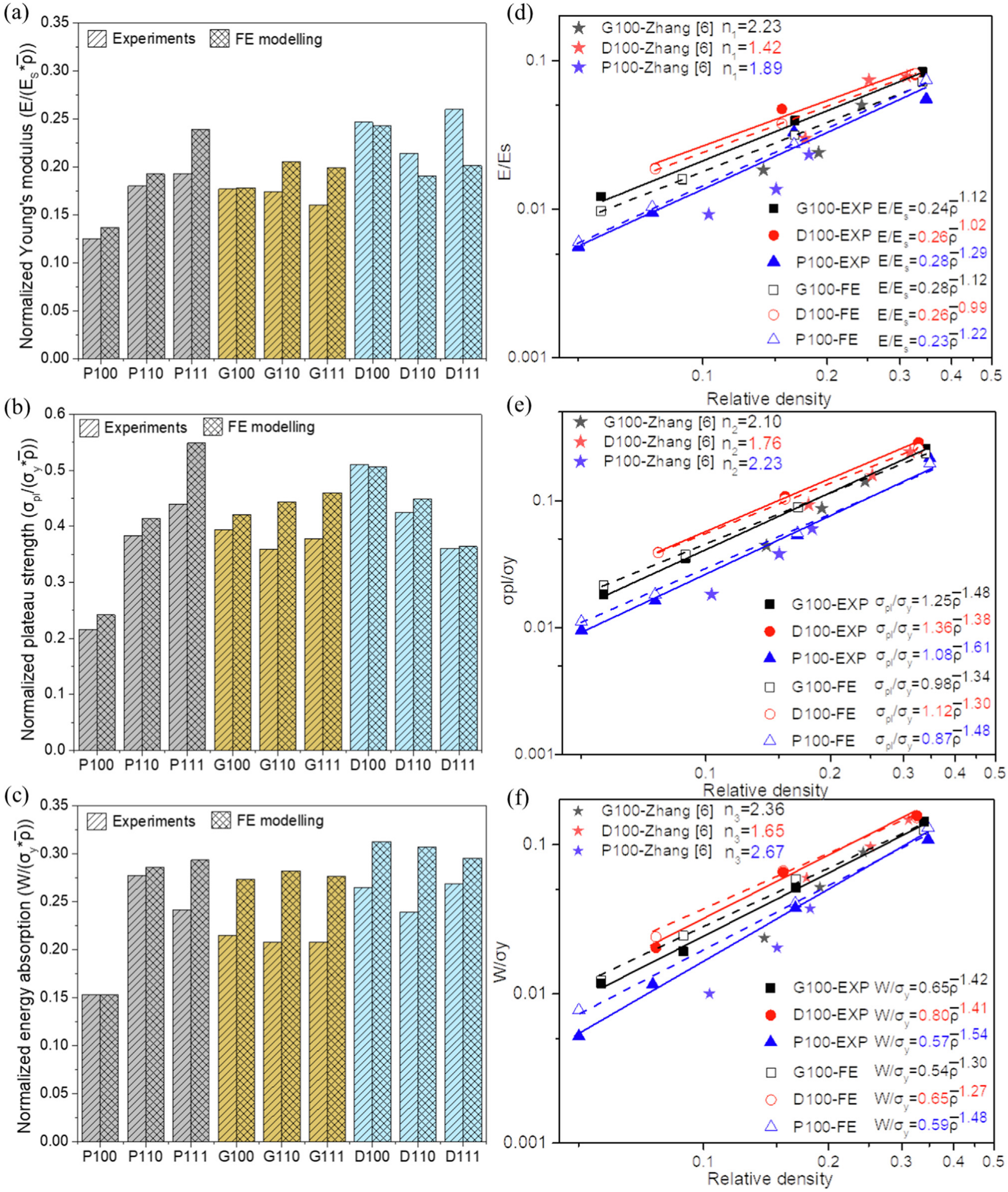

Fig. 9. Experimental and numerical normalized mechanical properties of as-printed TPMS shell lattices: (a, d) Young's modulus, (b, e) plateau strength, (c, f) absorbed energy. Mechanical properties in (a, b, c) belong to structures printed with a predefined relative density of 10%. Dash and solid lines in (d, e, f) are fitting lines using power laws. For comparison, (d, e, f) also illustrate the properties of TPMS structures fabricated by conventional LPBF as reported in [6].

rough surfaces, inherent gas pores and un-melted regions in the structures, which are induced by the LPBF process and hard to be completely avoided. With increasing relative density, the fitted lines tend to converge, and the discrepancy of the mechanical properties among the three types of TPMS gradually decreases and diminishes since the structure becomes more bulk-like.

Although the deformation modes are different at low and high relative density, the mechanical properties still show a nearly perfect power law fitting for the whole range of relative density. In contrast, Izard et al. [49] reported that the glassy carbon nanolattices with spinodal shell topology produced by two-photon direct laser writing exhibit distinct deformation modes, i.e., progressive failure for low-density structures and catastrophic failure for high-density counterparts, leading to different scaling behaviors at low and high relative density. The main difference between our and their work is the choice of the base material. Therefore, it can be concluded that the fabrication process as well as the property of base material could influence the scaling behavior of mechanical properties of cellular structures. It is the material SS316L and the μLPBF technology that offer TPMS structures such satisfactory light-weighting potential. On the other hand, all the three types of μLPBF TPMS structures present a stiffness exponent n_1 ranging between 1.02 ~ 1.29 and 0.99 ~ 1.22 for experimental and numerical results (Fig. 9 (d)), respectively, indicating a stretching-dominated behavior [42]. The exponents for strength n_2 and energy absorption n_3 fall within the range of 1.3 ~ 1.61 and 1.27 ~ 1.54 (Fig. 9 (e, f)), respectively. Interestingly, all of the three exponents fitted in this work are lower than the corresponding values of TPMS structures printed by conventional LPBF in [6], where the reported ranges of exponents n_1, n_2, n_3 were 1.42 ~ 1.33, 1.76 ~ 2.33 and 1.65 ~ 2.67, respectively. The lower n values of μLPBF TPMS structures indicate higher light-weighting potential. In addition, the mechanical properties are also higher than those in [6] for a specific relative density and TPMS type, as shown in Fig. 9 (d, e, f). Since the TPMS structures in this work were fabricated using the μLPBF system, where finer laser beam of 25 μm, and smaller powders of 0 ~25 μm were utilized, higher precision and less structural defects can be expected compared to those by conventional LPBF [16]. As a result, the high-quality TPMS structures in our work show higher mechanical properties and higher potential for lightweight design.

In this work, the D-type TPMS exhibits the smallest exponent values of n_1, n_2, n_3, while P-type TPMS has the largest values. Moreover, the D-type structures provides the highest stiffness, strength and toughness, while P-type one suggests the lowest mechanical properties. At lower relative density, D-type TPMS shows higher property superiority compared with the other two types. This indicates that D-type TPMS has the highest potential for lightweight designs. In addition, the TPMS structures fabricated by μLPBF present higher mechanical properties and better light-weighting potential as compared with those by conventional LPBF.

4. Conclusions

This work provides a combined experimental and numerical study to investigate the compressive responses of μLPBF fabricated SS316L TPMS shell lattices. The manufacturability of TPMS structures by μLPBF was analyzed in terms of surface quality, as-printed relative density and shell thickness. The deformation mechanisms and mechanical properties of TPMS shell lattices with respect to the relative densities, loading orientations and TPMS types were analyzed. The light-weighting potential of the TPMS structures related to the scaling of mechanical properties as a function of relative density was analyzed. The main findings are as follows:

(1) Various TPMS shell lattices with a wide range of relative density from 5 % to 40 % are successfully fabricated by μLPBF. Low-density TPMS structures with shell thickness as small as ~100 μm are realized. However, there is still inevitable deviation between the designed and measured shell thickness, which is more significant for low-density TPMS structures.
(2) The deformation mechanism is highly dependent on the relative density of the TPMS structures. With increasing relative density, the failure behavior and deformation mechanism of TPMS shell lattices change from localized shear bands or layer crushing behavior in low relative densities (<10 %) to homogeneous bulk deformation in moderate relative densities (20–40 %).
(3) For relative density of 10 %, P-type lattices show the highest anisotropy ratio of stiffness ($R_E = 1.54$), plateau strength ($R_\sigma = 2.04$) and energy absorption capability ($R_W = 1.81$), while G-type lattices are near-isotropic ($R_E = 1.11$, $R_\sigma = 1.10$, $R_W = 1.04$). D-type lattices have the highest mechanical properties and smallest scaling exponents for the three mechanical properties, showing the highest potential for lightweight designs.
(4) Compared with conventional LPBF, the TPMS shell lattices fabricated by μLPBF present higher mechanical properties, lower power law scaling exponents and thereby better light-weighting potential.

CRediT authorship contribution statement

Jin Fu: Conceptualization, Methodology, Software, Investigation, Validation, Visualization, Writing – original draft. **Junhao Ding:** Methodology, Investigation. **Shuo Qu:** Methodology, Investigation. **Lei Zhang:** Methodology, Validation. **Michael Yu Wang:** Supervision, Writing – review & editing. **M.W. Fu:** Conceptualization, Supervision, Funding acquisition, Writing – review & editing. **Xu Song:** Conceptualization, Supervision, Resources, Writing – review & editing.

Data availability

Data will be made available on request.

Declaration of Competing Interest

The authors declare that they have no known competing financial interests or personal relationships that could have appeared to influence the work reported in this paper.

Acknowledgements

The authors would like to thank GRF Project of 15228621 and Projects 1-ZE1W and 1-CD4H from The Hong Kong Polytechnic University. SONG Xu would like to acknowledge the financial support from the project #RNE-p2-21 of the Shun Hing Institute of Advanced Engineering, The Chinese University of Hong Kong.

Appendix A. Supplementary data

Supplementary data to this article can be found online at https://doi.org/10.1016/j.matdes.2022.111018.

References

[1] S.C. Han, J.W. Lee, K. Kang, A new type of low density material: shellular, Adv. Mater. 27 (37) (2015) 5506–5511.
[2] A.H. Schoen, Infinite periodic minimal surfaces without self-intersections, Natl. Aeronaut. Space Administrat. (1970).
[3] O. Al-Ketan, R.K. Abu Al-Rub, Multifunctional mechanical metamaterials based on triply periodic minimal surface lattices, Adv. Eng. Mater. 21 (2019) 1900524.
[4] S.C. Kapfer, S.T. Hyde, K. Mecke, C.H. Arns, G.E. Schröder-Turk, Minimal surface scaffold designs for tissue engineering, Biomaterials 32 (29) (2011) 6875–6882.
[5] O. Al-Ketan, R. Rowshan, R.K. Abu Al-Rub, Topology-mechanical property relationship of 3D printed strut, skeletal, and sheet based periodic metallic cellular materials, Addit. Manuf. 19 (2018) 167–183.
[6] L. Zhang, S. Feih, S. Daynes, S. Chang, M.Y. Wang, J. Wei, W.F. Lu, Energy absorption characteristics of metallic triply periodic minimal surface sheet structures under compressive loading, Addit. Manuf. 23 (2018) 505–515.

[7] D. Li, W. Liao, N. Dai, Y.M. Xie, Comparison of mechanical properties and energy absorption of sheet-based and strut-based gyroid cellular structures with graded densities, Materials 12 (2019) 2183.
[8] A.M. Abou-Ali, O. Al-Ketan, D.W. Lee, R. Rowshan, R.K. Abu Al-Rub, Mechanical behavior of polymeric selective laser sintered ligament and sheet based lattices of triply periodic minimal surface architectures, Mater. Des. 196 (2020) 109100.
[9] C. Crook, J. Bauer, A.G. Izard, C.S. de Oliveira, J.M.d.S. e Silva, J.B. Berger, L. Valdevit, Plate-nanolattices at the theoretical limit of stiffness and strength, Nat. Commun. 11 (2020) 1-11.
[10] X. Li, C.C. Roth, T. Tancogne-Dejean, D. Mohr, Rate- and temperature-dependent plasticity of additively manufactured stainless steel 316L: characterization, modeling and application to crushing of shell-lattices, Int. J. Impact. Eng. 145 (2020) 103671.
[11] Z. Xu, S.M.J. Razavi, M.R. Ayatollahi, Functionally graded lattice structures: fabrication methods, mechanical properties, failure mechanisms and applications, reference module in materials science and materials, Engineering (2022).
[12] M. Benedetti, A. du Plessis, R.O. Ritchie, M. Dallago, S.M.J. Razavi, F. Berto, Architected cellular materials: a review on their mechanical properties towards fatigue-tolerant design and fabrication, Mater. Sci. Eng. R Rep. 144 (2021) 100606.
[13] J. Fu, Z.H. Hu, X. Song, W. Zhai, Y. Long, H. Li, M.W. Fu, Micro selective laser melting of NiTi shape memory alloy: defects, microstructures and thermal/mechanical properties, Opt. Laser Technol. 131 (2020) 106374.
[14] S.B. Gao, Z.H. Hu, M. Duchamp, P.S.S.R. Krishnan, S. Tekumalla, X. Song, M. Seita, Recrystallization-based grain boundary engineering of 316L stainless steel produced via selective laser melting, Acta Mater. 200 (2020) 366–377.
[15] S. Qu, J. Ding, J. Fu, M. Fu, B. Zhang, X. Song, High-precision laser powder bed fusion processing of pure copper, Addit. Manuf. 48 (2021) 102417.
[16] S. Qu, J. Ding, X. Song, Achieving triply periodic minimal surface thin-walled structures by micro laser powder bed fusion process, Micromachines 12 (2021) 705.
[17] X. Song, W. Zhai, R. Huang, J. Fu, M.W. Fu, F. Li, Metal-Based 3D-Printed Micro Parts & Structures, in: F.G. Caballero (Ed.), Encyclopedia of Materials: Metals and Allloys, Elsevier, Oxford, 2022, pp. 448–461.
[18] A. Alhammadi, O. Al-Ketan, K.A. Khan, M. Ali, R. Rowshan, R.k., Abu Al-Rub, Microstructural characterization and thermomechanical behavior of additively manufactured AlSi10Mg sheet cellular materials, Mater. Sci. Eng., A 791 (2020) 139714.
[19] C.N. Kelly, J. Francovich, S. Julmi, D. Safranski, R.E. Guldberg, H.J. Maier, K. Gall, Fatigue behavior of As-built selective laser melted titanium scaffolds with sheet-based gyroid microarchitecture for bone tissue engineering, Acta Biomater. 94 (2019) 610–626.
[20] Y. Wang, X. Ren, Z. Chen, Y. Jiang, X. Cao, S. Fang, T. Zhao, Y. Li, D. Fang, Numerical and experimental studies on compressive behavior of Gyroid lattice cylindrical shells, Mater. Des. 186 (2020) 108340.
[21] J. Fu, S. Qu, J. Ding, X. Song, M.W. Fu, Comparison of the microstructure, mechanical properties and distortion of stainless steel 316 L fabricated by micro and conventional laser powder bed fusion, Addit. Manuf. 44 (2021) 102067.
[22] Q.P. Ma, L. Zhang, J.H. Ding, S. Qu, J. Fu, M.D. Zhou, M.W. Fu, X. Song, M.Y. Wang, Elastically-isotropic open-cell minimal surface shell lattices with superior stiffness via variable thickness design, Addit. Manuf. 47 (2021) 102293.
[23] D.W. Lee, K.A. Khan, R.K. Abu Al-Rub, Stiffness and yield strength of architectured foams based on the Schwarz Primitive triply periodic minimal surface, Int. J. Plast. 95 (2017) 1–20.
[24] B.D. Nguyen, S.C. Han, Y.C. Jung, K. Kang, Design of the P-surfaced shellular, an ultra-low density material with micro-architecture, Comput. Mater. Sci. 139 (2017) 162–178.
[25] H. Jia, H. Lei, P. Wang, J. Meng, C. Li, H. Zhou, X. Zhang, D. Fang, An experimental and numerical investigation of compressive response of designed Schwarz Primitive triply periodic minimal surface with non-uniform shell thickness, Extreme Mech. Lett. 37 (2020) 100671.
[26] I. Maskery, N.T. Aboulkhair, A.O. Aremu, C.J. Tuck, I.A. Ashcroft, Compressive failure modes and energy absorption in additively manufactured double gyroid lattices, Addit. Manuf. 16 (2017) 24–29.
[27] M. Zhao, D.Z. Zhang, F. Liu, Z. Li, Z. Ma, Z. Ren, Mechanical and energy absorption characteristics of additively manufactured functionally graded sheet lattice structures with minimal surfaces, Int. J. Mech. Sci. 167 (2020) 105262.
[28] X. Guo, J. Ding, X. Li, S. Qu, X. Song, J.Y.H. Fuh, W.F. Lu, W. Zhai, Enhancement in the mechanical behaviour of a Schwarz Primitive periodic minimal surface lattice structure design, Int. J. Mech. Sci. 216 (2022) 106977.
[29] C. Bonatti, D. Mohr, Smooth-shell metamaterials of cubic symmetry: Anisotropic elasticity, yield strength and specific energy absorption, Acta Mater. 164 (2019) 301–321.
[30] S. Rajagopalan, R.A. Robb, Schwarz meets Schwann: design and fabrication of biomorphic and durataxic tissue engineering scaffolds, Med. Image. Anal. 10 (2006) 693–712.
[31] A. Kumar, P.R. Dawson, Computational modeling of f.c.c. deformation textures over Rodrigues' space, Acta Mater. 48 (10) (2000) 2719–2736.
[32] I. Maskery, L. Sturm, A.O. Aremu, A. Panesar, C.B. Williams, C.J. Tuck, R.D. Wildman, I.A. Ashcroft, R.J.M. Hague, Insights into the mechanical properties of several triply periodic minimal surface lattice structures made by polymer additive manufacturing, Polymer 152 (2018) 62–71.
[33] H. Yin, X. Zheng, G. Wen, C. Zhang, Z. Wu, Design optimization of a novel bio-inspired 3D porous structure for crashworthiness, Compos. Struct. 255 (2021) 112897.
[34] S. AlMahri, R. Santiago, D.W. Lee, H. Ramos, H. Alabdouli, M. Alteneiji, Z.W. Guan, W. Cantwell, M. Alves, Evaluation of the dynamic response of triply periodic minimal surfaces subjected to high strain-rate compression, Addit. Manuf. 46 (2021) 102220.
[35] ISO 13314: 2011, Mechanical Testing of Metals-Ductility Testing-Compression Test for Porous and Cellular Metals, International Organization for Standardization, 2011.
[36] H. Yin, Z. Liu, J. Dai, G. Wen, C. Zhang, Crushing behavior and optimization of sheet-based 3D periodic cellular structures, Compos. B. Eng. 182 (2020) 107565.
[37] O. Al-Ketan, D.W. Lee, R. Rowshan, R.K. Abu Al-Rub, Functionally graded and multi-morphology sheet TPMS lattices: Design, manufacturing, and mechanical properties, J. Mech. Behav. Biomed. Mater. 102 (2020) 103520.
[38] M.F. Ashby, T. Evans, N.A. Fleck, J. Hutchinson, H. Wadley, L. Gibson, Metal foams: a design guide, Elsevier, 2000.
[39] J. Fu, H. Li, X. Song, M.W. Fu, Multi-scale defects in powder-based additively manufactured metals and alloys, J. Mater. Sci. Technol. 122 (2022) 165–199.
[40] L. Yang, S. Wu, C. Yan, P. Chen, L. Zhang, C. Han, C. Cai, S. Wen, Y. Zhou, Y. Shi, Fatigue properties of Ti-6Al-4V Gyroid graded lattice structures fabricated by laser powder bed fusion with lateral loading, Addit. Manuf. 46 (2021) 102214.
[41] M.F. Ashby, The properties of foams and lattices, Philos. Trans. A Math. Phys. Eng. Sci. 364 (2006) 15–30.
[42] T. Maconachie, M. Leary, B. Lozanovski, X.Z. Zhang, M. Qian, O. Faruque, M. Brandt, SLM lattice structures: properties, performance, applications and challenges, Mater. Des. 183 (2019) 108137.
[43] Y.M. Wang, T. Voisin, J.T. McKeown, J. Ye, N.P. Calta, Z. Li, Z. Zeng, Y. Zhang, W. Chen, T.T. Roehling, R.T. Ott, M.K. Santala, P. Depond, M.J. Matthews, A.V. Hamza, T. Zhu, Additively manufactured hierarchical stainless steels with high strength and ductility, Nat. Mater. 17 (1) (2018) 63–71.
[44] D. Downing, A. Jones, M. Brandt, M. Leary, Increased efficiency gyroid structures by tailored material distribution, Mater. Des. 197 (2021) 109096.
[45] C. Qiu, S. Yue, N.J.E. Adkins, M. Ward, H. Hassanin, P.D. Lee, P.J. Withers, M.M. Attallah, Influence of processing conditions on strut structure and compressive properties of cellular lattice structures fabricated by selective laser melting, Mater. Sci. Eng., A 628 (2015) 188–197.
[46] M.-S. Pham, C. Liu, I. Todd, J. Lertthanasarn, Damage-tolerant architected materials inspired by crystal microstructure, Nature 565 (7739) (2019) 305–311.
[47] Q.M. Li, I. Magkiriadis, J.J. Harrigan, Compressive strain at the onset of densification of cellular solids, J. Cell. Plast. 42 (5) (2006) 371–392.
[48] L.J. Gibson, M.F. Ashby, Cellular Solids: Structure and Properties, Cambridge University Press, Cambridge, 1997.
[49] A. Guell Izard, J. Bauer, C. Crook, V. Turlo, L. Valdevit, Ultrahigh Energy Absorption Multifunctional Spinodal Nanoarchitectures, Small 15 (2019) e1903834.